Electrochimica Acta 464 (2023) 142927

Contents lists available at ScienceDirect

Electrochimica Acta

journal homepage: www.journals.elsevier.com/electrochimica-acta

A doped cobaltite for enhanced SOFCs fed with dry biogas

Sebastian Vecino-Mantilla, Massimiliano Lo Faro *

Institute of Advanced Energy Technologies (ITAE) of the Italian National Research Council (CNR), Via Salita S. Lucia sopra Contesse 5, 98126 Messina, Italy

ARTICLE INFO

Keywords:
Green deal
Perovskite
Electrochemistry
Gas-to-power
Renewable

ABSTRACT

Solid oxide fuel cells are suggested as potential devices for revolutionizing the way electric power is produced for stationary and mobile uses. While this technology has made significant progress since its first demonstration in the 1980s, certain issues still need to be resolved, primarily the flexibility in using fuels, especially those derived from biological sources. To address this issue, we proposed the use of a modified perovskite material, $La_{1.5}Sr_{1.5}Co_{1.5}Ni_{0.5}O_{7\pm\delta}$ (LSCN), which offers enhanced resistance to carbon cracking while preserving the existing manufacturing chain and electrical performance of commercial cells.

A combination of physicochemical, morphological, and electrochemical experiments provided insight into the behaviour of LSCN. Its key strengths included excellent performance (*e.g.* > 650 mW cm^{-2}) and no significant carbon deposits on the anode and LSCN during 400-hour testing of a coated commercial cell. The analysis of in-depth changes in the LSCN surface and bulk after thermochemical treatments indicated that this material can be seamlessly integrated with commercial cells.

1. Introduction

Energy markets today consider biofuels as an interesting energy source. Conventional thermal engines are almost exclusively used to convert biofuels into power. As these engines operate inefficiently, especially when they burn biogas, which has a high CO_2 content, they can significantly impact the environment, both in terms of noise and pollutants. Additionally, nitrogen and sulfur compounds, which are generally present in biofuels, can adversely affect the lifetime of such engines. Alternatives to thermal engines include fuel cells, which use an electrochemical process that is highly efficient and possesses a selective mechanism that excludes inert species. Although all fuel cell types offer advantages over traditional thermal engines, Solid Oxide Fuel Cells (SOFCs) exhibit the highest potential for converting biofuels to power due to their high operating temperatures and conversion kinetics [1,2]. In addition, the materials used in this kind of cells are relatively cost-effective to other fuel-cell-based technologies. Currently, SOFCs have significant commercial potential in a wide range of applications in different fields, including portable and stationary energy solutions.[3] This is because of the SOFCs intrinsic fuel flexibility, electrical and conversion efficiencies, low pollution emissions, and modularity which enables the sizing of this technology according to specific needs [4].

Commercial SOFCs commonly use ZrO_2 stabilised with Y_2O_3 (YSZ) as an electrolyte to enable selective oxygen ion conductivity at high temperatures [5]. A variety of materials have been used for the cathode, including doped manganites, cobaltites, and ferrites [6,7]. For the anode, Ni-YSZ is used, which is most often used as a cell support (anode supporting cells, or ASCs) [7].

Despite the fact that Ni is highly electrically conductive, mechanically stable, and has favourable manufacturing properties, it also catalyzes carbon formation (coking) when dry hydrocarbon fuels are directly fed into the cell, which negatively affects the microstructure and lifespan of the cell [7].

While these issues exist, and there is research underway for fully ceramic or Ni-free alternatives, commercial cells continue to use Ni-YSZ anodes because of their well-established manufacturing process [8,9]. Even so, the challenge in this field remains developing competitive materials, or anode protective layers, that can enhance fuel flexibility while limiting deactivation mechanisms by promoting alternative reactions compatible with the behaviour of commercial cells. Cermets containing bimetallic alloys and doped ceria have already advanced the field in this area[10–16]. As cermets are both thermally and electrically compatible with commercial anodes, the use of these materials could lead to real technological advances. However, perovskite showing mixed ionic electronic conducting (MIEC) properties are also considered as anode materials and coatings for commercial SOFCs. Materials like these can be modulated to extend triple phase boundaries (TPBs), break bonds between C-H, C-C, and C=C, and resist sulfur poisoning, allowing

---

* Corresponding author.
E-mail address: lofaro@itae.cnr.it (M. Lo Faro).

https://doi.org/10.1016/j.electacta.2023.142927
Received 9 May 2023; Received in revised form 11 July 2023; Accepted 20 July 2023

them to be used as anodes fed with fuels other than hydrogen[17–23]. However, MIEC materials need improvements in both their catalytic and electrical properties to compete with conventional anodes, although they will probably never achieve the same level of Ni-YSZ's electronic conductivity [24,25]. Nevertheless, it is still possible for MIECs to have enhanced electrochemical properties and catalytic performance if they contain active metal nanoparticles on the surface. Such morphologies are probably most easily realized by impregnating MIEC materials with precursors of active metals followed by post-annealing. As a result, fine nanoparticles may be distributed irregularly on the surface of MIEC [25, 26]. An alternative approach would be to dissolve active metals in their oxidized forms in the electrode material during synthesis. In the presence of a reducing atmosphere, high temperatures, and certain conditions, such as A-site defects, B-site element segregation can occur, allowing nanosized metallic particles to segregate from the bulk to the surface. This mechanism is called *in situ* growth or exsolution [27–29]. A similar method has been extensively applied to the fabrication of perovskites[19,30], as well as Ruddlesden-Popper (RP) phases [31], resulting in a homogeneous dispersion of active metals that facilitate fuel oxidation, improving electronic conduction, reducing carbon formation, and even reducing coarsening difficulties[26,27,32,33]. Ni doping has been extensively studied in Fe- and Mn-based perovskites or RP phases as SOFC anodes [19,34-37]. Contrary to this, Co-based perovskites doped with Ni remain underexplored despite their interesting redox properties.

However, several aspects support this possibility:

-Co-based perovskites have lower electrochemical overpotentials compared to Fe- or Mn-based perovskites;

-Co has a similar catalytic performance to Ni, but induces less carbon formation and deposition, even when high-hydrocarbon fuels (*e.g.* C_3H_8) are used [38];

-Co nanoparticles could easily precipitate at lower temperatures, leading to less coarsening of the microstructure, thus extending the cell's lifespan [39,40].

-B-site doping with Co instead of Mn in these crystal structures enhances the O^{2-} transport and the electrocatalytic activity [41].

Recently, a novel RP phase material, $La_{1.5}Sr_{1.5}Mn_{1.5}Ni_{0.5}O_{7\pm\delta}$ (*i.e.* LSMN n= 2, two perovskite units between rock-salt layers based on $La_{1-x}Sr_xO$), was developed. Under reducing conditions and at high temperatures (>750°C), this material has been exposed to complete Ni exsolution, thereby transforming the original oxide matrix into a novel RP ($LaSrMnO_{4\pm\delta}$ or LSM n=1, one perovskite unit between rock-salt layers also based on $La_{1-x}Sr_xO$). The result was fine, stable, and well-distributed nickel-based nanoparticles on the surface of the RP. From synthesis methodology to characterization of materials to catalytic tests in the presence of natural gas, these studies provided essential information. As a result of its superior catalytic performance and resistance to carbon formation [31,33,42], LSMN was used as a protective coating layer on the anode side of commercial SOFCs fed with dry biogas. Electrochemical experiments showed that well-designed catalytic formulations coated on conventional cells can mitigate problems associated with the use of dry organic fuels [34].

Consequently, considering the characteristics of Co as a B-site dopant instead of Mn, this paper examines a possible novel material as a coating layer for commercial anode-supported SOFCs. Thus, this study characterized $La_{1.5}Sr_{1.5}Co_{1.5}Ni_{0.5}O_{7\pm\delta}$ (LSCN) thoroughly and examinedits electrochemical behaviour towards the electrooxidation of dry biogas (CH_4, 60 mol% and CO_2, 40 mol% [43]) over a long period to establish its potential use as a coating layer in commercial SOFCs.

2. Materials and methods

Synthesis

By using stoichiometric amounts of $La(NO_3)_3.6H_2O$ (≥ 99.9 % Alfa), $Sr(NO_3)_2$ (≥ 99 % Aldrich), $Co(NO_3)_2.6H_2O$ (≥99.99 % Aldrich) and Ni $(NO_3)_2.6H_2O$ (≥ 99.999 % Aldrich), LSCN powder was synthesized by the Pechini method (citrate complexation route) [44]. First, the solution of citric acid (CA, >99.5% Sigma-Aldrich) was used as the starting aqueous solution for dissolving the precursors in a molar ratio of CA:(metal ion)total = 3:1. Using a hot plate, the solution was slowly heated from room temperature to 120°C under constant stirring. Then, ethylene glycol (≥ 99 %, Aldrich) was added as a polymerizing agent (1.5 mL per gram of targeted product). Gel formation was induced by heating the solution to 150°C. Following the drying step, the gel was annealed in the air for two dwell times at 300°C for 2 hours and 500°C for 3 hours to ensure complete removal of organic components. The resulting powders were calcined at 1000°C for six hours, 1100°C for six hours, and 1300°C for twelve hours with a ramp rate of 2°C min^{-1}.

To obtain the final electrocatalyst, the as-calcined LSCN powders (70 wt.%) were ground together with 30 wt.% of commercial gadolinia doped ceria (*i.e.* $Ce_{0.9}Gd_{0.1}O_2$) using a ball mill for 6 h at 250 RPM with ethanol to avoid extreme friction in the jar. Based on previous studies with perovskites-based electrocatalysts, 10% gadolinium-doped ceria was selected for its remarkable ability to store and release oxygen ions (spillover) and its acceptable electrical conductivity[23,37,45-47].

Material characterization

An in-depth study of the physical and chemical properties of LSCN was performed on both fresh and used samples. Using the ALTAMIRA AMI-300 equipment, a series of cycles involving first reduction (TPR), post-oxidation (TPO), and second reduction (TPR) were performed to evaluate the redox properties of LSCN. In these analyses, 5% H_2 in Ar (TPR) and 5% O_2 in Ar (TPO) were fed into the system heated from room temperature to 850°C at a ramp rate of 10°C min^{-1}. In each case, the structure of specimens was analyzed with a Bruker D8 ADVANCE diffractometer with Cu Kα radiation, operating at 40 kV and 40 mA. Using the native software of the XRD equipment, the spectra were analyzed, and phases were assigned using the Crystallography Open Database (COD). The specimen morphology was examined with an FEI XL 30 Scanning Electron Microscope (SEM).

The surface behaviour of specimens was evaluated using a Physical Electronics (PHI) 5800-01 spectrometer equipped with a monochromatic Al Kα X-ray source (XPS). The XPS spectra were post-analyzed using the instrument's native software, while the bands were assigned using the literature and NIST X-ray Photoelectron Spectroscopy Database.

Cell preparation, electrochemical set-up, and electrochemical characterization

To obtain the final slurry for deposition onto a commercial cell, the LSCN-CGO mixture was ground for 2 h with organic additives (8 wt. % terpineol, 2 wt. % polyvinyl butyral resin (BUTVAR B-98) and 2-propanol). A fairly robust button cell with an active area of 1 cm^2 (ASC1) manufactured by InDEC® was used in this study. Its composition was Ni-YSZ/YSZ/LSM (where YSZ refers to $(ZrO_2)_{0.92}(Y_2O_3)_{0.08}$ and LSM refers to $La_{0.8}Sr_{0.2}MnO_3$) and was designed to operate optimally at temperatures above 800°C. A cell of this type was selected since it was derived from the same large-area cell used in our previous experiments concerning InDEC® bare and coated cells[34,48].

In order to ensure optimal cell contact with external electrochemical equipment, a layer of gold paste was applied to both electrodes and then annealed at 500°C for 10 minutes. After that, the slurry of LSCN-CGO was brush-painted on the anode and post-annealed at 500°C to burn the organic additives. The final loading of LSCN-CGO was 13 mg cm^{-2} based on weighting the cell before and after deposition. A pair of gold wires were then welded to each electrode to collect both current and voltage. As a final step, the cell was sealed with a ceramic paste (AREMCO 316) at the end of an alumina tube, with the anode exposed to the inner side of the tube and the cathode exposed to static air.

Finally, this assembly (*i.e.* alumina tube, cell, and electrical contact) was placed in a tubular furnace for prolonged operation at high temperatures as depicted in Figure S1(supplementary materials). The sealing paste was cured before electrochemical testing according to the procedure provided by AREMCO. The cell was then pre-conditioned in diluted H_2 (50% in He) at 800°C for 12 h. Following pre-conditioning, the cell was put into operation. Initially, the cell operated with diluted H_2 (60% in He) as a baseline, and then with dry simulated biogas at a total flow rate of F=15 $cm^3\ min^{-1}$ (CH_4, 9 $cm^3\ min^{-1}$ and CO_2, 6 $cm^3\ min^{-1}$). Electrochemical studies included measurements of open circuit voltage (OCV), polarization curves (current-potential, I-V curves), impedance spectroscopy (EIS) and long-duration galvanostatic measurement using a BioLogic diagnostic tool equipped with a 100 A booster and frequency response analyser module for impedance spectroscopy. To determine the anodic outlet gas quality, a Thermostar® equipment (from PFEIFFER Vacuum) capable of measuring masses up to 300 amu was used.

3. Results

LSCN was initially analyzed by coupling TPR/TPO/TPR analyses with XRD acquisitions to explore its redox behaviour. Since H_2, O^{2-}, and electric current are circulated between the anode and cathode, the anode or its protective layer must be flexible and reversible. This part of the study was designed to gain insight into the consequences of simulated anodic mechanisms in LSCN structures. Consequently, Fig. 1 displays the temperature-programmed analyses. The first analysis highlighted five reduction events occurring at different temperatures and consuming different amounts of H_2. In addition to indicating the type of metal involved, these evidences provided insight into its initial and final oxidation state. Literature indicates that the broad band centred at 288°C (α^I) corresponded to the transition from Co^{4+} to Co^{3+}[49]. The transition from Co^{3+} to Co^{2+} occurred around 405°C (α^{II}), which consumed a similar amount of H_2 as in the signal at lower temperatures. Around 616°C (α^{III}), Co^{2+} is reduced to metallic Co with about twice as much H_2 as at lower temperatures. Based on the literature, these reduction events primarily involved the surface of LSCN [50,51]. In contrast, the broadband at 795°C (γ) was due to the bulk reduction of Co [49,52]. Instead, the signal centred at 456°C (β) involved the reduction of Ni^{2+} to metallic Ni [50], and the H_2 consumption was similar to that seen for α^{III}.

According to the TPO analysis, Ni and Co have undergone reverse transformations in the LSCN. In this analysis, an equal number of TPR chemical events were observed, some of which remained at the same position, while others narrowed or shifted at lower temperatures. Typically, the peak at intermediate temperatures (220-550°C) indicated with ω occurs at or near the surface of Co due to its re-oxidation to Co^{4+} [53–56]. Moreover, the peak at 518°C (χ) is from the reoxidation of the bulk of Co [53], and it was much narrower than its corresponding reduction peak, indicating a faster and simpler mechanism than the initial reduction. Furthermore, Ni re-oxidation occurred at 432°C (ψ), lower than the corresponding reduction temperature [56,57]. Therefore, it could be argued that this redox mechanism altered the morphology of the LSCN due to the lower energy required for the re-oxidation of Ni and bulk Co.

A second TPR round significantly simplified the profile of LSCN's reduction compared with the first. A slow reduction event between 180-340°C (α^I) formed a noticeable shoulder in the TPR profile, followed by two sharp peaks at 417°C and 692°C (γ). At high temperatures, the peak is solely attributed to the bulk reduction of Co, while at intermediate temperatures, the peak is a combination of partial and complete reductions of Co and Ni (α^{II}, α^{III}, and β). As an outcome of this second TPR, it can be argued that aside from the transition from Co^{4+} to Co^{3+}, where the transition took place at a slower rate but essentially with similar energy (α^I), all of the remaining reduction events took place at lower temperatures and were more energetically favourable.

Fig. 2 shows the XRD results of the LSCN after it has been calcined and after the redox reactions have taken place. Rietveld refinement was used to analyze the spectrum of the as-calcined LSCN and revealed two structures leading to Co-based perovskites (*i.e.* $La_{0.5}Sr_{0.5}CoO_3$) identified with the COD card n. 152-5854 [58] and Ni-based Ruddlesden-Popper phase (*i.e.* $La_{0.5}Sr_{0.5}NiO_4$) identified with the COD card n. 152-1323 [59]. In addition to these two main phases, the sample calcined at 1300°C for 12 hours had a couple of spurious reflections, including the one at 28°. These reflections can be attributed to slightly different lattice structures caused by defective stoichiometries or, most probably, to the coexistence of Co and Ni (*e.g.* in other words, one of these would have to be at the doping level) in the B-sites of perovskite and RP phases. The phase composition was estimated at 65.5 wt.% as RP phase and 34.5 wt.% as perovskite. With reflections from both phases co-existing in the same regions, estimating crystallite size using Debye-Sherrer equations was difficult.

According to the multiple phases observed, after the first TPR, the structure of reduced LSCN was fully altered. There was evidence of phases La_2O_3 (COD card n 200-2287), SrO (COD card n 900-8727), Ni (COD card n 210-0658), and Co (COD card n 153-4891). In addition to these four phases, no other structures could be recognised in the XRD spectrum of LSMN after the first TPR. This finding confirmed the results of the first TPR, where Co and Ni were completely reduced within the investigated temperature range, while La_2O_3 and SrO remained in their oxide form because they require more energy to become metallic.

The LSCN powder re-oxidised by TPO analysis is the next profile to be discussed. Spectrum analysis indicates that the patterns were similar to those of the as-calcined sample, though the purity of this sample has been enhanced, as indicated by the absence of the peak at 28°. According to the Rietveld refinement, the phase composition was also slightly altered, resulting in 79.6 wt.% as the RP phase and 20.4 wt.% as

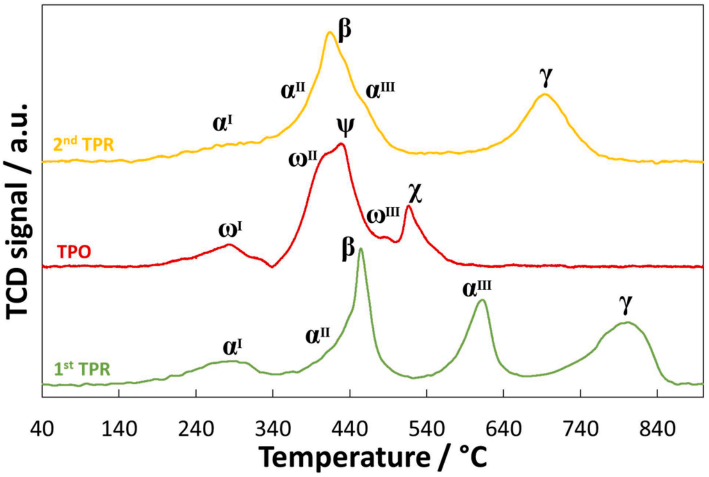

Fig. 1. The profiles of three thermal program analyses for the LSCN electrocatalyst.

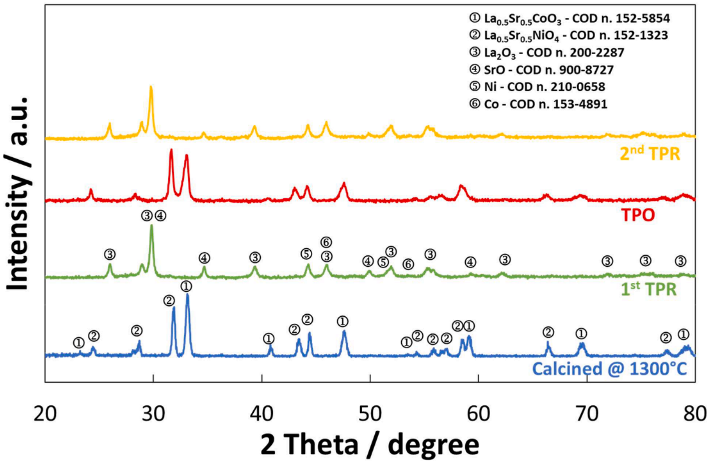

Fig. 2. Results of XRD analyses conducted on LSCN after a thermochemical treatment cycle.

the perovskite phase. The peaks also appeared less narrowed, suggesting crystallites with smaller sizes, although their evaluation through the Debye-Sherrer equation was challenging.

When the LSCN electrocatalyst was reduced a second time, the TPR profile differed from the first reduction (see Fig. 1), but it substantially replicated the same XRD profile. These combined experiments (*i.e.* TPR/TPO/TPR and XRDs) demonstrated stable redox behaviour in the material, thereby making it a suitable candidate for SOFC's anodic applications.

The LSCN-CGO electrocatalyst was used in this study to improve the fuel flexibility of a commercial cell. An evaluation of galvanostatic durability was conducted at 800°C and shown in Fig. 3. A baseline experiment of 200 mA cm^{-2} was conducted in diluted H_2 for approximately 65 h to establish a baseline for experimental characterization of the cell in the presence of dry biogas. During this period, the cell potential partly declined, probably due to coarsening of Ni in the anode, resulting in reduced electronic percolation. It is not surprising that this behaviour occurs at high temperatures (800°C) since the experiment was carried out at such a high temperature. The cell was then fed dry biogas at 500 mA cm^{-2} and remained in these conditions for about 385 h (*i.e.* 16 days) before being placed again in diluted H_2 for a concluding characterization. This period was marked by gradual, but sluggish, improvements in performance. A fascinating feature of this trend was that it remained stable for a long period, proving that it has the potential for improving commercial cells' fuel flexibility. However, this trend was lost when the cell was fed again with diluted H_2.

An in-depth diagnosis was performed to better understand this interesting behaviour. Nearly every day, polarization curves and impedance spectra were collected and analyzed (see Figure S3 in the supplementary materials), although only a few of them are shown in the following figures illustrating the general trend of cell behaviour. The diagnosis included an analysis of three additional redox cycles with multiple fixed current densities under steady-state conditions. Analyzing the anodic outlet gas, together with these tests, provided information about reaction mechanisms (see Table S1 and Figure S2 in the supplementary materials). In response to repeated diagnostic procedures based on redox cycles, the cell returned optimally to its previous performance. It was further proof of the robustness of this cell type and of the design for enhancing fuel flexibility.

Fig. 4 shows some of the polarization curves collected throughout the lifetime of the cell. The maximum power density achieved after preconditioning was 718 mW cm^{-2} @ 0.6V, which is substantially in line with the performance of a bare cell of this type as reported in the literature. Immediately following the switch to dry biogas operation, the maximum power of the cell dropped to 575 mW cm^{-2} @ 0.6 V. However, as shown in Fig. 3, the durability test recorded a gradual and consistent improvement in the cell's performance, with a maximum power density of 700 mW cm^{-2} @ 0.6 V after 385 h, only 2% less than the maximum power density recorded at the beginning of the electrochemical test with diluted hydrogen.

Following the return to diluted H_2 feeding in the anode, the cell showed a slightly lower power density (680 mW cm^{-2} @ 0.6 V). Despite the differences in the maximum power densities, it was interesting to examine how the I-V curves behaved. A maximum OCV of 960 mV was

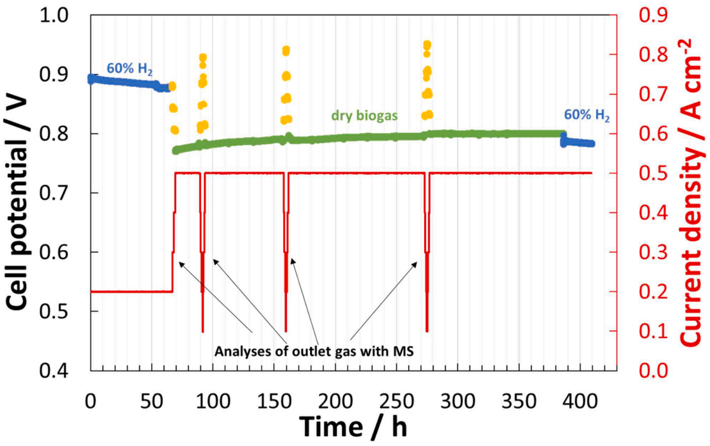

Fig. 3. Cell durability testing performed at 800°C under galvanostatic conditions.

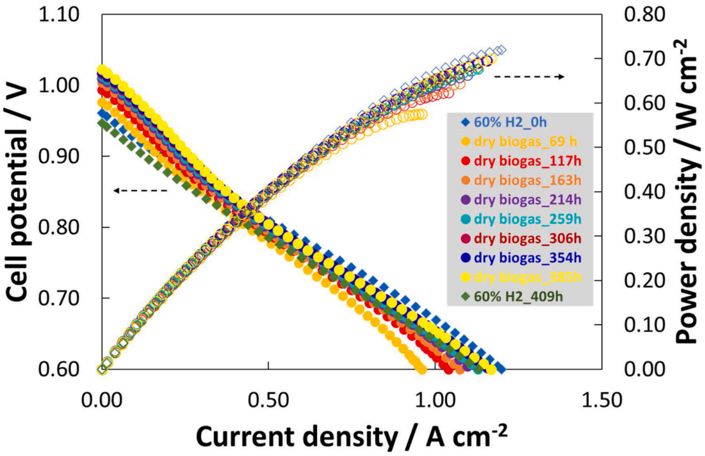

Fig. 4. Polarization curves of the cell measured over the course of its lifetime at 800°C.

observed under diluted H_2, a value considered quite low when compared to the values generally observed for a cell of this type, which are generally in the range of 1.03-1.10 Volts, depending on the sealing characteristics, electrical connections quality, and of course the fuel dilution and its reactivity with the anode electrocatalyst. However, this relatively low OCV value could be due to the additional coating layer applied to the cell, as observed in earlier experiments [34,48]. However, it was interesting to observe that the OCV gradually increased when biogas was fed, and along with it, the performance of the cell as well. As soon as the diluted H_2 was re-fed into the cell, the OCV was low again, similar to that initially recorded.

Despite this, the cell's performance at practical potentials (*e.g.* 0.8-0.7 V) remained substantially constant throughout the period and independently of the fuel type, proving that the cell was stable and reliable even in the presence of dry biogas.

The first-order derivatives of I-V curves are shown in Fig. 5 to better highlight the variations in the I-V curve characteristics over time. In this figure, the Area Specific Resistance (ASR) is plotted over the cell current density. Based on the graph, the cell fed with dilute H_2 demonstrated a high initial activation constraint (*e.g.* the curve at the lowest current density). The perovskites layer might have caused this effect since these materials are typically more active towards different reactions than direct H_2 electrooxidation. As shown in Fig. 5, the curves for the biogas-fed cell showed a different trend. Over time, the activation loss decreased from its initial value. The ASR immediately after switching to biogas was 0.44 ohm cm^2 and dropped to 0.33 ohm cm^2 after 385 h of operation. Increasing ohmic loss accompanied a trend in the ASR at low current density. As a result of prolonged biogas operation, the ASR peak moved toward higher current densities. As soon as the cell switched to biogas, the maximum ASR was around 70 mA cm^{-2}, which increased to 200 mA cm^{-2} after 385 h.

Afterwards, the slope rapidly declines, indicating favourable conditions between 450 and 700 mA cm^{-2}. Then, cell performance was heavily influenced by reactant diffusion at high current densities. A direct correlation was also found between the ageing of cells and the trend of the curves at high current densities. According to this experiment, the curve features were associated with a cell that was always less affected by diffusion control over time.

This trend may be explained by the dry oxidation of methane causing an increase in the partial pressures of intermediates according to the following reaction

$$CH_4 + CO_2 \rightarrow 2CO + 2H_2 \qquad \text{(reaction 1)}$$

Once these catalytic products have diffused over the triple phase boundary (TPB) of the anode, they can be electrochemically oxidized by combining with oxygen ions from the cathode and releasing electrons in the external electrical circuit:

$$2CO + 2H_2 + 4O^{2-} \rightarrow 2CO_2 + 2H_2O + 8e^- \qquad \text{(reaction 2)}$$

As a result of this reaction, the partial pressure of CO_2 and H_2O in the anodic chamber increases, but it can also lead to catalytic steam reforming in the catalytic sites of the anode composed of Ni-YSZ or in the pre-layer:

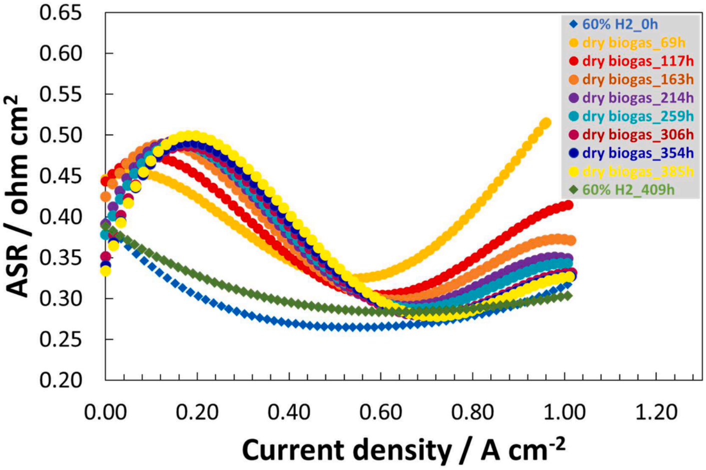

Fig. 5. Area Specific Resistance (ASR) vs current density, computed as a first order derivative of the I-V curves (Fig. 4).

$$CH_4 + H_2O \rightarrow CO + 3H_2 \quad \text{(reaction 3)}$$

Consequently, biogas can result in multiple reactions and a mass spectrometer was used during this electrochemical experiment to uncover possible reaction mechanisms. Even so, the most interesting aspect of this study was how the cracking reaction (equation 4) was apparently inhibited, which would be detrimental to commercial cells.

$$CH_4 \rightarrow C + 2H_2 \quad \text{(reaction 4)}$$

The cracking of methane produces two moles of H_2. These can be converted electrochemically to two molecules of water and, as a result, a steam-to-carbon ratio of 2 is probably set in the anode and could be quite acceptable for the steam reforming of methane. Despite this, practical conditions generally require an excess of fuel. In practical terms, this poses a serious threat to cell resilience if as in this case, no water is fed. In this research, the cell was fed approximately 10 times more methane than required by the faradic equation at 500 mA cm^{-2} for the complete oxidation of methane. Thus, this approach was a huge challenge for this cell design, and the shuttle mechanism described in a previous paper may be responsible for its apparent resilience [37].

The screening also included an EIS analysis at 800 mV and 700 mV, which are generally within the operating potential ranges of commercial SOFCs. According to Fig. 6, the series resistance (R_s) of cells increased with time. Essentially, such a term is derived from the intercept between the EIS spectrum at high frequency and the x-axis. A similar behaviour would be expected in commercial SOFCs operating at high temperatures due to the coalescence of Ni. An increase in particle size leads to a reduction in electronic percolation, resulting in an increase in the R_s of the cell. These spectra are also notable for the number of quasi-semicircles present. In the case of the cell fed with H_2, there were two well-defined quasi-semicircles and one minor semicircle at the lowest frequencies, as observed at the beginning and end of the durability test. The spectra of the biogas-fed cell, on the other hand, showed three well-defined quasi-semicircles, especially at 800 mV (Fig. 6a). These spectra also showed that changes in fuel type mostly affected quasi-semicircles at intermediate and low frequencies (see Table S1 and Figure S3 in the supplementary materials).

Every quasi-semicircle in an EIS spectrum of a complete cell corresponds to one electrochemical reaction occurring at the electrodes. Depending on the characteristic reaction mechanism involved, the quasi-semicircle had a slightly depressed appearance. The frequency at which quasi-semicircles appear is an indication of reaction kinetics. Therefore, complete cells usually exhibit faster reactions at higher frequency semicircles.

It was evident from the feature of EIS spectra in Fig. 6 that the spectra did not change significantly at high frequencies as fuel types changed. As a result, it seems more likely that the first quasi-semicircle was caused by a reaction involving oxygen reduction, which is quite efficient at 800°C using LSM as an electrocatalyst. Also, H_2 oxidation is fast, and in principle, it would be faster than oxygen reduction. However, it is possible that a coating layer that contains an oxide (LSCN-CGO) could slow this process, and this behaviour matches the relatively low OCV recorded for the diluted H_2-fed cell (see Fig. 4).

There is also the presence of a third well-defined semicircle at low frequency, suggesting either a poorly optimised TPB or the direct oxidation of a fuel containing many electrons. As for the first possibility, it could be a result of low TPBs extending into the coating layer. There is little chance of this happening since the partial pressure of oxygen ions at such a wide physical distance from the electrolyte should be negligible. Furthermore, there was a gold layer between the anode and the coating layer that substantially blocked any ions travelling from the cathode to the anode. Therefore, it is evident that the coating layer had a role in the pre-catalytic mechanism.

Regarding the second possibility, a low-frequency semicircle could result directly from direct methane oxidation. As a matter of fact, while H_2 and CO, which are produced by reactions 1 and 3, can be oxidized by simply combining with 1 oxygen ion and releasing 2 electrons:

$$H_2 + O^{2-} \rightarrow H_2O + 2e^- \quad \text{(reaction 5)}$$

$$CO + O^{2-} \rightarrow CO_2 + 2e^- \quad \text{(reaction 6)}$$

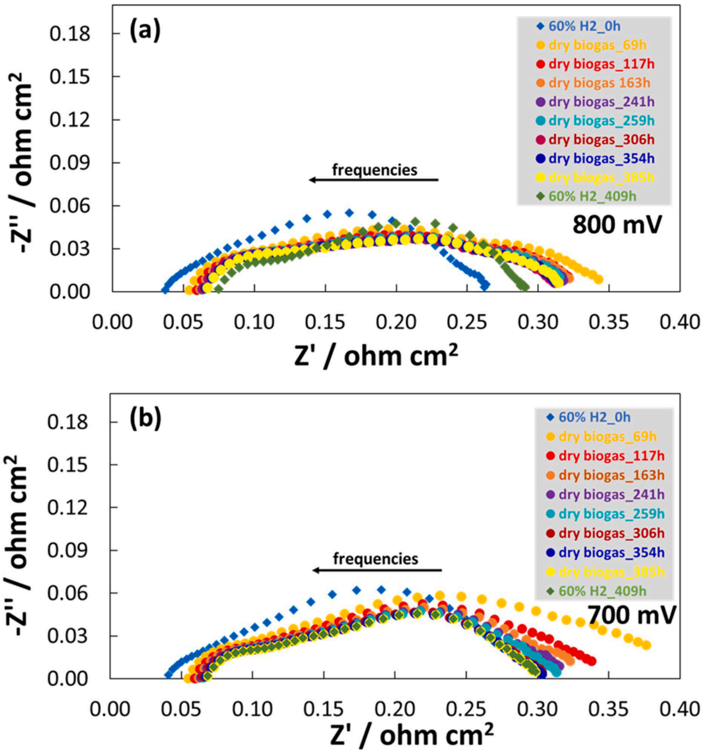

Fig. 6. Cell impedance spectra measured at 800 mV (a) and 700 mV (b) during its lifetime.

they ought to behave similarly to anodes based on Ni. But, for methane oxidation, four oxygen ions are needed and eight electrons must be released:

$$CH_4 + 4O^{2-} \rightarrow CO_2 + 2H_2O + 8e^- \qquad \text{(reaction 7)}$$

In light of this, it is obvious to consider that the low frequency was probably caused by the direct oxidation of methane.

The spectra collected at 700 mV (Fig. 6b) showed a similar trend to those collected at 800 mV. Similarly, R_s increased over time while the intercept between the x-axis and spectrum at low frequency, which is designed as total resistance (R_t), decreased over time.

In conjunction with this reduction of R_t, the quasi-semicircle appearing at lower frequencies is depleted. These results may be explained by the saturation of electrocatalytic sites with H_2 and CO, which results in a reduction of methane partial pressure over the electrocatalytic sites. Moreover, the humidity in the anodic chamber was improved as well as the likelihood of methane being reformed by steam.

As shown in Fig. 7, the LSCN-CGO electrocatalyst was studied under three different conditions, including calcination at 1300°C, reduction at 800°C to simulate electrocatalyst behaviour when reduced, and prolonged operation as a coating layer during the cell electrochemical experiment discussed above. As a result of the limited sample obtained from the cell experiment (*i.e.* used sample), the XPS analysis, in this case, was quite noisy. Surveys of these XPS analyses are presented in the supplementary materials (Figure S4, supplementary materials). Using quantitative analysis of survey results, it was found that the reducing treatment enriched Sr on the surface, while carbon content in the spent sample did not increase significantly.

Fig. 7 presents the multiplex analysis of the main elements in the specimens. For the three samples compared, the spectra for the electronic structure of C showed different behaviours. The spent catalyst had two significant peaks in addition to the adventitious carbon peak (284.6 eV) used for spectra alignment. As reported in the literature, the peak at 285.72 eV could be described as CO adsorbed on Co [60], while the peak

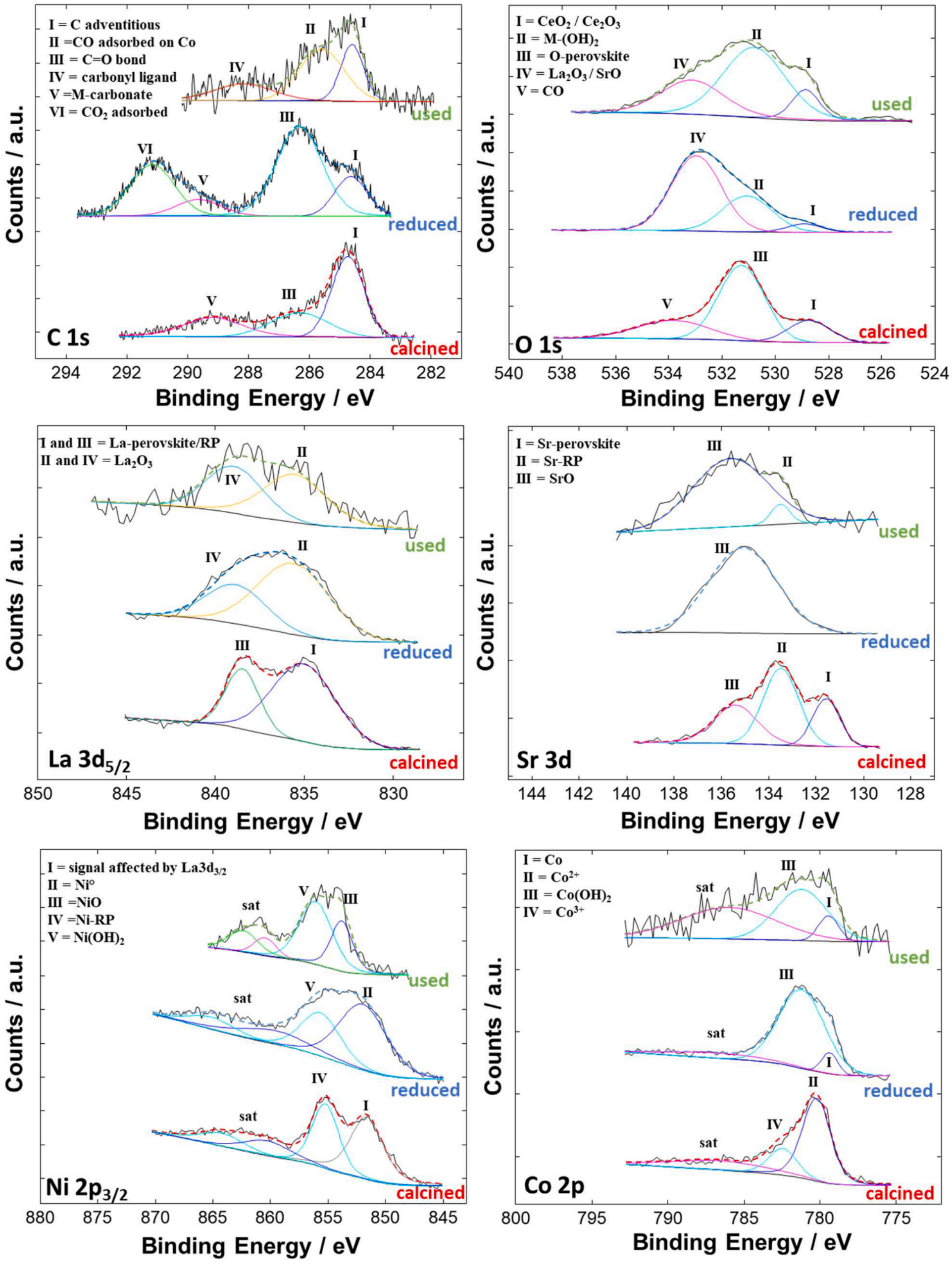

Fig. 7. XPS studies of the LSCN's main elements in response to thermal and chemical treatments.

at 288.34 eV was assigned to carbonyl-based ligand [61]. Carbides and soot were not observed in any significant amounts. These types of carbon typically exhibit lower energy signals than adventitious carbons [61–63]. Regarding the other two samples, the as-calcined sample showed peaks at 286.33 eV for the carbonyl group [64] and 289.17 eV for the carbonates [65]. In addition to these two peaks, the as-reduced sample also showed a peak at higher binding energy (*i.e.* 291.16 eV) associated with adsorbed CO_2 [66].

Analysis of the electronic structure of oxygen provided additional information about the LSCN-CGO electrocatalyst after thermal and chemical treatments. Additionally to the typical oxygen signal of oxygen bonded with cerium between 528.6 - 529.60 eV, we observed two additional peaks. The oxygen peak moved into this range because of the redox behaviour of cerium [67]. Upon calcining, the electrocatalyst showed a typical perovskite oxygen peak at 531.26 eV [68] and a carbonyl peak at 533.83 eV [69]. Additionally, the reduced and spent electrocatalysts showed two signals at 532.8 eV associated with La_2O_3 [70] which confirmed the XRD spectrum, and 531.05 eV associated with metal hydroxides at the surface [71]. The peaks recognised for the reduced and spent electrocatalysts were essentially similar, with the only difference being their relative intensities. Based on this observation, the spent catalyst operated with a reduced surface, even if the relative amount of species changed due to the more complex environment (*e.g.* water, CO, and hydrocarbons) compared to the reduced sample.

In the as-calcined sample, $La3d_{5/2}$ spectra showed typical spin-orbit doublet peaks shifting at low energy (*i.e.* 834.4 eV and 837.8 eV) related to La^{3+} embedded in perovskites or RP phases [72]. After the LSCN was treated, lanthanum signals moved towards higher energies in the region generally corresponding to La_2O_3 [73].

With regards to the electronic configuration of Sr3d, this exhibited in the as-calcined sample the typical structure of an oxide mainly embedded in the perovskite and Ruddlesden-Popper phases. This specific case revealed a well-defined electronic structure for Sr within these two phases. There was one peak at 131.4 eV due to Sr in the perovskite [74], and another at 133.47 eV due to Sr in the RP phase [75]. As can be seen from the area of these peaks, Sr is primarily enriched in the RP phase. The reduced sample showed essentially the peak of SrO, while the spent catalyst also showed the peak for Sr in the RP phase, in addition to the peak of SrO. Substantially, as indicated by the electronic structure of Sr in the spent electrocatalyst, LSCN may return to perovskite and RP when conditions are appropriate.

The presence of $La3d_{3/2}$ adversely interfered with the study of the electronic structure of Ni. Nevertheless, the electronic structure of Ni on the as-calcined sample consisted of a peak centred at 855.21 eV due to its presence in an RP phase [76], whereas the reduced and spent samples showed a signal slightly moved to a higher energy level due to Ni-hydroxide [76]. There was, however, a difference between the electronic structure of Ni in reduced and spent samples. The reduced sample showed a sharp peak centred around 852 eV due to metallic Ni [77], while the spent catalyst showed a slight peak at 853.81 eV due to NiO [78], which is probably due to traces of H_2O remaining in the anode chamber during cooling to ambient temperature.

Two peaks and one satellite were observed in the spectrum of Co, which is consistent with the existence of Co^{3+} and Co^{2+} in the sample as calcined [79]. While the electronic structures of the reduced and spent samples for Co were similar, there were some differences in the relative amounts between these species. There was a clear signal for metallic Co by the peak at 778,5 eV [80], although there was also a peak for Co-hydroxide at 781 eV [76]. According to XPS results, the LSCN electrocatalyst exhibited redox properties, consistent with the TPR-TPO-TPR cycle and XRD results.

In order to highlight the effect of the prolonged operation on the cell's microstructure, a transversal cut was made on the spent cell for microscopical examination. In Fig. 8a, each layer is shown at low magnification, with arrows indicating the material type. The magnification made it possible to detect no significant damage to the cell. This image also shows where the electric contacts were placed for measuring cell potential and current. As described in the experimental part, gold contacts were directly connected to the cathode LSM and anode Ni-YSZ, while the coating layer covered the anodic contact layer. Thus, the LSCN-CGO in this case served as a pre-catalytic layer, as the TPB phase

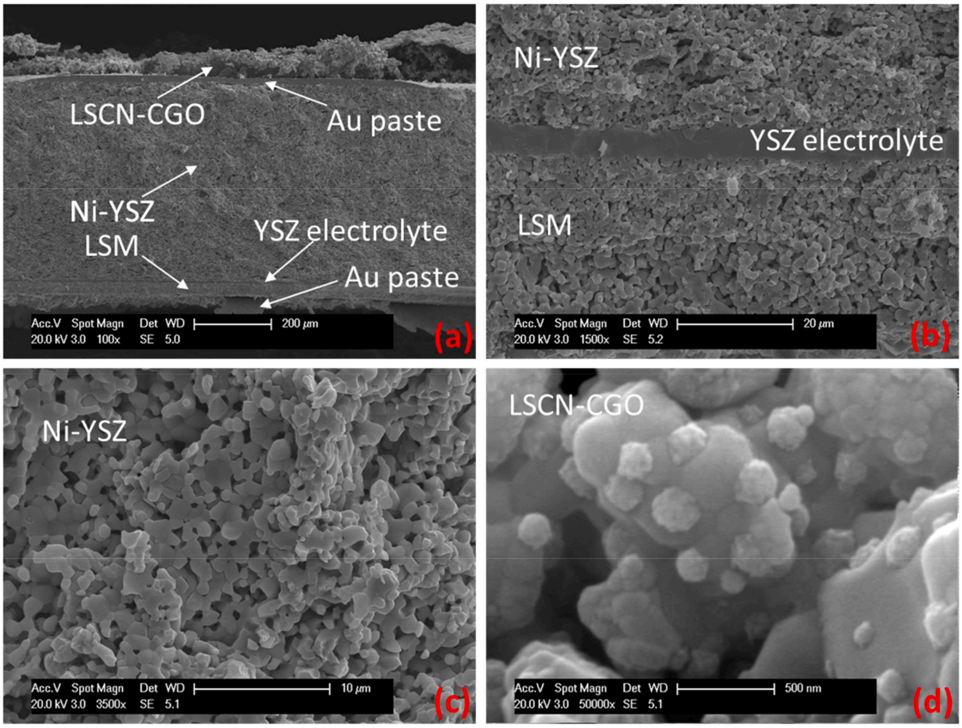

Fig. 8. SEM images showing the spent cell at different magnifications and in different zones in particular depicting the complete cell (a), the electrolyte-electrode interfaces (b), the anode layer (c), and the coating layer (d).

was negligible at this distance from the electrolyte. Since the coated cell was prepared using a brush painting technique, the thickness of the precatalytic layer varied from 39-87 μm.

In Fig. 8b, the electrolyte-electrode interfaces are illustrated in more detail. At this magnification, the spent cell showed no damage to the interfaces, proving that this specific type of cell is quite robust and can likely be operated for a much longer period than examined here. A portion of the anode can be seen in Fig. 8c. The microstructure of this electrode was found to be uniform, but there was also a slight agglomeration of particles, which could explain the initial performance loss. But as discussed, this type of cell operates at such high temperatures that a limited coarsening of Ni is almost physiological. However, the most interesting aspect was finding that there were no traces of carbon soot. Regarding this, it should be noted that the cell was discharged in the presence of diluted H_2 as it had operated during the last period of the durability test. As a result, it is possible that carbon soot was oxidized by either H_2O or high reactive O-ions during the durability test with diluted H_2.

A magnified image of the coating layer can be seen in Fig. 8d. As part of the microstructure of this layer, fine LSCN particles with spherical and dendrimeric aspect with an average size of 185 nm were supported or encapsulated on CGO. Similar distributions of materials might prevent particle coalescence, although perovskites are not as susceptible to this mechanism as the Ni of the anode. Aside from that, the "exotic" morphology of this electrocatalyst may have a higher surface area than smooth spherical particles. It might also be one of the reasons why the cell showed high stability and optimal performance when operated with dry biogas.

Conclusions

In order to improve the ability of a commercial SOFC to convert organic fuels into electrical energy, a perovskite-based material was investigated as a potential coating layer for the SOFC's anode. Based on a combination of physico-chemical experiments including TPR-TPO-TPR analyses, XRD and XPS scans, which determined the behaviour of the material in both the bulk and on its surface, this study examined the redox behaviour of a material with the chemical formula $La_{1.5}Sr_{1.5}Co_{1.5}Ni_{0.5}O_{7\pm\delta}$ (LSCN). The electrochemical studies demonstrated that a commercial cell coated with this material is capable of delivering excellent performance and can also withstand degradation mechanisms including methane cracking, as predicted by the experimental conditions. It was apparent from viewing the spent cell microstructure that this type of cell was very robust, while the LSCN shape appeared to be highly resistant to coalescence, as demonstrated by its fine dimensions and dendritic structure shown after prolonged operation at 800°C and high current density.

CRediT authorship contribution statement

Sebastian Vecino-Mantilla: Investigation, Writing – original draft, Formal analysis. **Massimiliano Lo Faro:** Funding acquisition, Project administration, Conceptualization, Supervision, Writing – review & editing.

Declaration of Competing Interest

The authors declare that they have no known competing financial interests or personal relationships that could have appeared to influence the work reported in this paper.

Data availability

Data will be made available on request.

Acknowledgements

This research was funded by the European Union – NextGeneration EU from the Italian Ministry of Environment and Energy Security POR H2 AdP MMES/ENEA with involvement of CNR and RSE, PNRR - Mission 2, Component 2, Investment 3.5 "Ricerca e sviluppo sull'idrogeno", CUP: B93C22000630006.

Dr Lo Faro acknowledges the ITELECTROLAB, the Joint lab between CNR-ITAE and IQSC-USP financed by the National Research Council of Italy (CNR) and the bilateral project "FlexPower- Solid Oxide Fuel Cell fed with Biofuel as an Electric Flexible Provider in a Distributed Grid" granted by MAECI.

Supplementary materials

Supplementary material associated with this article can be found, in the online version, at doi:10.1016/j.electacta.2023.142927.

References

[1] O. Yamamoto, Solid oxide fuel cells: fundamental aspects and prospects, Electrochimica Acta 45 (2000) 2423–2435.

[2] S.A. Saadabadi, A. Thallam Thattai, L. Fan, R.E.F. Lindeboom, H. Spanjers, P. V. Aravind, Solid Oxide Fuel Cells fuelled with biogas: Potential and constraints, Renewable Energy 134 (2019) 194–214.

[3] G. Brunaccini, Chapter 8 - Solid oxide fuel cell systems, in: M. Lo Faro (Ed.), Solid Oxide-Based Electrochemical Devices, Academic Press, 2020, pp. 251–293.

[4] M.J. López-Robledo, M.A. Laguna-Bercero, A. Larrea, V.M. Orera, Reversible operation of microtubular solid oxide cells using La0.6Sr0.4Co0.2Fe0.8O3-δ-Ce0.9Gd0.1O2-δ oxygen electrodes, Journal of Power Sources 378 (2018) 184–189.

[5] P. Zhang, M. Shen, The role of cobalt on cathode material for intermediate temperature solid oxide fuel cells: A review, International Journal of Hydrogen Energy (2022).

[6] H. Sumi, T. Yamaguchi, K. Hamamoto, T. Suzuki, Y. Fujishiro, High performance of La0.6Sr0.4Co0.2Fe0.8O3–Ce0.9Gd0.1O1.95 nanoparticulate cathode for intermediate temperature microtubular solid oxide fuel cells, Journal of Power Sources 226 (2013) 354–358.

[7] Z. Jamil, E. Ruiz-Trejo, P. Boldrin, N.P. Brandon, Anode fabrication for solid oxide fuel cells: Electroless and electrodeposition of nickel and silver into doped ceria scaffolds, International Journal of Hydrogen Energy 41 (2016) 9627–9637.

[8] B. Song, E. Ruiz-Trejo, A. Bertei, N.P. Brandon, Quantification of the degradation of Ni-YSZ anodes upon redox cycling, Journal of Power Sources 374 (2018) 61–68.

[9] M. Pihlatie, T. Ramos, A. Kaiser, Testing and improving the redox stability of Ni-based solid oxide fuel cells, Journal of Power Sources 193 (2009) 322–330.

[10] Y.M. Park, H. Kim, An additional layer in an anode support for internal reforming of methane for solid oxide fuel cells, International Journal of Hydrogen Energy (2014) 16513–16523.

[11] M. Lo Faro, R.M. Reis, G.G.A. Saglietti, A.G. Sato, E.A. Ticianelli, S.C. Zignani, A. S. Aricò, Nickel-Copper/Gadolinium-doped Ceria (CGO) composite electrocatalyst as a protective layer for a Solid-Oxide Fuel Cell anode fed with ethanol, ChemElectroChem 1 (2014) 1395–1402.

[12] M. Lo Faro, R.M. Reis, G.G.A. Saglietti, S.C. Zignani, S. Trocino, P. Frontera, P. L. Antonucci, E.A. Ticianelli, A.S. Aricò, Investigation of Ni-based alloy/CGO electro-catalysts as protective layer for a solid oxide fuel cell anode fed with ethanol, Journal of Applied Electrochemistry 45 (2015) 647–656.

[13] H.J. Kim, B.C. Yang, J. Lee, S.E. Jo, G. Park, S. Ji, J. An, Co-Sputtered Pt-Ru Catalytic Functional Layer for Direct-Methane Fueled Low Temperature Solid Oxide Fuel Cells, Journal of the Korean Society for Precision Engineering 39 (2022) 91–95.

[14] Z. Lyu, Y. Wang, Y. Zhang, M. Han, Solid oxide fuel cells fueled by simulated biogas: Comparison of anode modification by infiltration and reforming catalytic layer, Chemical Engineering Journal (2020) 393.

[15] M. LoFaro, S. Trocino, S.C. Zignani, C. Italiano, R.M. Reis, E.A. Ticianelli, A. S. Aricò, Nickel–Iron/Gadolinium-doped Ceria (CGO) composite electrocatalyst as a protective layer for a Solid-Oxide Fuel Cell anode fed with biofuels, ChemCatChem 8 (2016) 648–655.

[16] S.H. Lee, H. Kim, Dual layered anode support for the internal reforming of methane for solid oxide fuel cells, Ceramics International 40 (2014) 5959–5966.

[17] M.V. Sandoval, C. Pirovano, E. Capoen, R. Jooris, F. Porcher, P. Roussel, G. H. Gauthier, In-depth study of the Ruddlesden-Popper LaxSr2−xMnO4±δ family as possible electrode materials for symmetrical SOFC, International Journal of Hydrogen Energy 42 (2017) 21930–21943.

[18] M. Lo Faro, S. Campagna Zignani, A.S. Aricò, Lanthanum Ferrites-Based Exsolved Perovskites as Fuel-Flexible Anode for Solid Oxide Fuel Cells 13 (2020) 3231.

[19] T. Zhu, H.E. Troiani, L.V. Mogni, M. Han, S.A. Barnett, Ni-Substituted Sr(Ti,Fe)O3 SOFC Anodes: Achieving High Performance via Metal Alloy Nanoparticle Exsolution, Joule 2 (2018) 478–496.

[20] P. Qiu, L. Wu, K. Cheng, S. Wu, H. Qi, C. Xiong, B. Tu, Ni-doped Ba0.9Zr0.8Y0.2O3-δ as a methane dry reforming catalyst for direct CH4–CO2 solid oxide fuel cells, International Journal of Hydrogen Energy (2023).

[21] Q. Xu, Z. Guo, L. Xia, Q. He, Z. Li, I. Temitope Bello, K. Zheng, M. Ni, A comprehensive review of solid oxide fuel cells operating on various promising alternative fuels, Energy Conversion and Management 253 (2022), 115175.

[22] K.M. Dunst, J. Karczewski, T. Miruszewski, B. Kusz, M. Gazda, S. Molin, P. Jasinski, Investigation of functional layers of solid oxide fuel cell anodes for synthetic biogas reforming, Solid State Ionics 251 (2013) 70–77.

[23] M. Lo Faro, V. Modafferi, P. Frontera, P. Antonucci, A.S. Aricò, Catalytic behavior of Ni-modified perovskite and doped ceria composite catalyst for the conversion of odorized propane to syngas, Fuel Processing Technology 113 (2013) 28–33.

[24] B. Shri Prakash, S. Senthil Kumar, S.T. Aruna, Properties and development of Ni/YSZ as an anode material in solid oxide fuel cell: A review, Renewable and Sustainable Energy Reviews 36 (2014) 149–179.

[25] J. Shen, G. Yang, Z. Zhang, W. Zhou, W. Wang, Z. Shao, Tuning layer-structured La0.6Sr1.4MnO4+δ into a promising electrode for intermediate-temperature symmetrical solid oxide fuel cells through surface modification, Journal of Materials Chemistry A 4 (2016) 10641–10649.

[26] L. Thommy, O. Joubert, J. Hamon, M.-T. Caldes, Impregnation versus exsolution: Using metal catalysts to improve electrocatalytic properties of LSCM-based anodes operating at 600°C, International Journal of Hydrogen Energy 41 (2016) 14207–14216.

[27] C. Xu, W. Sun, R. Ren, X. Yang, M. Ma, J. Qiao, Z. Wang, S. Zhen, K. Sun, A highly active and carbon-tolerant anode decorated with in situ grown cobalt nano-catalyst for intermediate-temperature solid oxide fuel cells, Applied Catalysis B: Environmental 282 (2021), 119553.

[28] R. Glaser, T. Zhu, H. Troiani, A. Caneiro, L. Mogni, S. Barnett, The enhanced electrochemical response of Sr(Ti0.3Fe0.7Ru0.07)O3−δ anodes due to exsolved Ru–Fe nanoparticles, Journal of Materials Chemistry A 6 (2018) 5193–5201.

[29] D. Neagu, G. Tsekouras, D.N. Miller, H. Ménard, J.T.S. Irvine, In situ growth of nanoparticles through control of non-stoichiometry, Nature Chemistry 5 (2013) 916–923.

[30] Y. Gao, D. Chen, M. Saccoccio, Z. Lu, F. Ciucci, From material design to mechanism study: Nanoscale Ni exsolution on a highly active A-site deficient anode material for solid oxide fuel cells, Nano Energy 27 (2016) 499–508.

[31] S. Vecino-Mantilla, P. Gauthier-Maradei, M. Huvé, J.M. Serra, P. Roussel, G. H. Gauthier, Nickel Exsolution-Driven Phase Transformation from an n=2 to an n=1 Ruddlesden-Popper Manganite for Methane Steam Reforming Reaction in SOFC Conditions, ChemCatChem 11 (2019) 4631–4641.

[32] C. Arrivé, T. Delahaye, O. Joubert, G. Gauthier, Exsolution of nickel nanoparticles at the surface of a conducting titanate as potential hydrogen electrode material for solid oxide electrochemical cells, Journal of Power Sources 223 (2013) 341–348.

[33] S. Vecino-Mantilla, P. Simon, M. Huvé, G. Gauthier, P. Gauthier-Maradei, Methane steam reforming in water-deficient conditions on a new Ni-exsolved Ruddlesden-Popper manganite: Coke formation and H2S poisoning, International Journal of Hydrogen Energy 45 (2020) 27145–27159.

[34] S. Vecino-Mantilla, S.C. Zignani, R.-N. Vannier, A.S. Aricò, M.Lo Faro, Insights on a Ruddlesden-Popper phase as an active layer for a solid oxide fuel cell fed with dry biogas, Renewable Energy (2022).

[35] J.J. Lee, K. Kim, K.J. Kim, H.J. Kim, Y.M. Lee, T.H. Shin, J.W. Han, K.T. Lee, In-situ exsolution of Ni nanoparticles to achieve an active and stable solid oxide fuel cell anode catalyst on A-site deficient La0.4Sr0.4Ti0.94Ni0.06O3-δ, Journal of Industrial and Engineering Chemistry 103 (2021) 264–274.

[36] J. Feng, G. Yang, N. Dai, Z. Wang, W. Sun, D. Rooney, J. Qiao, K. Sun, Investigation into the effect of Fe-site substitution on the performance of Sr2Fe1.5Mo0.5O6−δ anodes for SOFCs, Journal of Materials Chemistry A 2 (2014) 17628–17634.

[37] M. Lo Faro, R.M. Reis, G.G.A. Saglietti, V.L. Oliveira, S.C. Zignani, S. Trocino, S. Maisano, E.A. Ticianelli, N. Hodnik, F. Ruiz-Zepeda, A.S. Aricò, Solid oxide fuel cells fed with dry ethanol: The effect of a perovskite protective anodic layer containing dispersed Ni-alloy @ FeOx core-shell nanoparticles, Applied Catalysis B: Environmental 220 (2018) 98–110.

[38] C. Yang, J. Li, Y. Lin, J. Liu, F. Chen, M. Liu, In situ fabrication of CoFe alloy nanoparticles structured (Pr0.4Sr0.6)3(Fe0.85Nb0.15)2O7 ceramic anode for direct hydrocarbon solid oxide fuel cells, Nano Energy 11 (2015) 704–710.

[39] K.-Y. Lai, A. Manthiram, Evolution of Exsolved Nanoparticles on a Perovskite Oxide Surface during a Redox Process, Chemistry of Materials 30 (2018) 2838–2847.

[40] K.-Y. Lai, A. Manthiram, Self-Regenerating Co–Fe Nanoparticles on Perovskite Oxides as a Hydrocarbon Fuel Oxidation Catalyst in Solid Oxide Fuel Cells, Chemistry of Materials 30 (2018) 2515–2525.

[41] X. Pan, Z. Wang, B. He, S. Wang, X. Wu, C. Xia, Effect of Co doping on the electrochemical properties of Sr2Fe1.5Mo0.5O6 electrode for solid oxide fuel cell, International Journal of Hydrogen Energy 38 (2013) 4108–4115.

[42] S. Vecino-Mantilla, E. Quintero, C. Fonseca, G.H. Gauthier, P. Gauthier-Maradei, Catalytic steam reforming of natural gas over a new Ni exsolved Ruddlesden-Popper manganite in SOFC anode conditions, ChemCatChem 12 (2020) 1453–1466.

[43] N. Kamalimeera, V. Kirubakaran, Prospects and restraints in biogas fed SOFC for rural energization: A critical review in indian perspective, Renewable and Sustainable Energy Reviews 143 (2021), 110914.

[44] M.P. Pechini, Method of preparing lead and alkaline earth titanates and niobates and coating method using the same to form a capacitor, Google Patents, 1967.

[45] M. Lo Faro, D. La Rosa, I. Nicotera, V. Antonucci, A.S. Arico, Electrochemical investigation of a propane-fed solid oxide fuel cell based on a composite Ni-perovskite anode catalyst, Applied Catalysis B-Environmental 89 (2009) 49–57.

[46] M. Lo Faro, M. Minutoli, G. Monforte, V. Antonucci, A.S. Arico, Glycerol oxidation in solid oxide fuel cells based on a Ni-perovskite electrocatalyst, Biomass & Bioenergy 35 (2011) 1075–1084.

[47] M. Lo Faro, A.S. Arico, Electrochemical behaviour of an all-perovskite-based intermediate temperature solid oxide fuel cell, International Journal of Hydrogen Energy 38 (2013) 14773–14778.

[48] M. Santoro, E. Di Bartolomeo, I. Luisetto, A.S. Aricò, G. Squadrito, S.C. Zignani, M. Lo Faro, Insights on the electrochemical performance of indirect internal reforming of biogas into a solid oxide fuel cell, Electrochimica Acta (2022) 409.

[49] D. Pinto, A. Glisenti, Pulsed reactivity on LaCoO3-based perovskites: a comprehensive approach to elucidate the CO oxidation mechanism and the effect of dopants, Catalysis Science & Technology 9 (2019) 2749–2757.

[50] R. Li, D. Li, L. Wang, Q. Zhou, J. Li, X. Yu, J. Liu, Z. Zhao, Effects of different B-site ions on the catalytic performance of 3DOM LaBO3 for the simultaneous elimination of NOx and soot particulates from diesel engines, Chemical Physics Impact 6 (2023), 100135.

[51] S. Wang, J. Zhu, S.A.C. Carabineiro, P. Xiao, Y. Zhu, Selective etching of in-situ formed La2O3 particles to prepare porous LaCoO3 perovskite for catalytic combustion of ethyl acetate, Applied Catalysis A: General 635 (2022), 118554.

[52] J. Li, Q. Liu, Y. Song, H. Lv, W. Feng, Y. Shen, C. Guan, X. Zhang, G. Wang, In-situ exsolution of cobalt nanoparticles from La0.5Sr0.5Fe0.8Co0.2O3-δ cathode for enhanced CO2 electrolysis performance, Green Chemical Engineering 3 (2022) 250–258.

[53] N. Tien-Thao, H. Alamdari, S. Kaliaguine, Characterization and reactivity of nanoscale La(Co,Cu)O3 perovskite catalyst precursors for CO hydrogenation, Journal of Solid State Chemistry 181 (2008) 2006–2019.

[54] A.A. Ansari, S.F. Adil, M. Alam, N. Ahmad, M.E. Assal, J.P. Labis, A. Alwarthan, Catalytic performance of the Ce-doped LaCoO3 perovskite nanoparticles, Scientific Reports 10 (2020) 15012.

[55] M.C. Stoian, C. Romanițan, G. Crăciun, D.C. Culiță, F. Papa, M. Badea, C. Negrilă, I. Popescu, I.-C. Marcu, Multicationic LDH-derived Co(x)CeMgAlO mixed oxide catalysts for the total oxidation of methane, Applied Catalysis A: General 650 (2023), 119001.

[56] P. Błaszczak, M. Zając, A. Ducka, K. Matlak, B. Wolanin, S.-F. Wang, A. Mandziak, B. Bochentyn, P. Jasiński, High-temperature Co-electrolysis of CO2/H2O and direct methanation over Co-impregnated SOEC. Bimetallic synergy between Co and Ni, International Journal of Hydrogen Energy 47 (2022) 35017–35037.

[57] N. Ahmad, R. Wahab, S. Manoharadas, B.F. Alrayes, F. Alharthi, Utilization of Greenhouse Gases for Syngas Production by Dry Reforming Process Using Reduced BaNiO3 Perovskite as a Catalyst, Sustainability 13 (2021) 13855.

[58] A. Das, S.K. Paranjpe, P.A. Joy, S.K. Date, Neutron depolarization and diffraction studies in cluster glass La0.5Sr0.5CoO3, Journal of Alloys and Compounds 326 (2001) 101–104.

[59] J.E. Millburn, M.A. Green, D.A. Neumann, M.J. Rosseinsky, Evolution of the Structure of the K2NiF4 Phases La2−xSrxNiO4+δ with Oxidation State: Octahedral Distortion and Phase Separation (0.2≤x≤1.0), Journal of Solid State Chemistry 145 (1999) 401–420.

[60] D.A. Wesner, G. Linden, H.P. Bonzel, Alkali promotion on cobalt: Surface analysis of the effects of potassium on carbon monoxide adsorption and Fischer-Tropsch reaction, Applied Surface Science 26 (1986) 335–356.

[61] U. Gelius, P.F. Hedén, J. Hedman, B.J. Lindberg, R. Manne, R. Nordberg, C. Nordling, K. Siegbahn, Molecular Spectroscopy by Means of ESCA III. Carbon compounds, Physica Scripta 2 (1970) 70.

[62] S. Sinharoy, L.L. Levenson, The formation and decomposition of nickel carbide in evaporated nickel films on graphite, Thin Solid Films 53 (1978) 31–36.

[63] R.I.R. Blyth, H. Buqa, F.P. Netzer, M.G. Ramsey, J.O. Besenhard, P. Golob, M. Winter, XPS studies of graphite electrode materials for lithium ion batteries, Applied Surface Science 167 (2000) 99–106.

[64] H. Binder, D. Sellmann, Röntgen-photoelektronenspektroskopische Untersuchungen an Pentacarbonyl- Chrom-und -Wolfram-Komplexen mit Stickstoffliganden /X-ray Photoelectron Studies of Pentacarbonyl Chromium and Tungsten Complexes with Nitrogen Ligands, Zeitschrift für Naturforschung B 33 (1978) 173–179.

[65] R.P. Vasquez, X-ray photoelectron spectroscopy study of Sr and Ba compounds, Journal of Electron Spectroscopy and Related Phenomena 56 (1991) 217–240.

[66] G. Illing, D. Heskett, E.W. Plummer, H.J. Freund, J. Somers, T. Lindner, A. M. Bradshaw, U. Buskotte, M. Neumann, U. Starke, K. Heinz, P.L. De Andres, D. Saldin, J.B. Pendry, Adsorption and reaction of CO2 on Ni{110}: X-ray photoemission, near-edge X-ray absorption fine-structure and diffuse leed studies, Surface Science 206 (1988) 1–19.

[67] T.L. Barr, C.G. Fries, F. Cariati, J.C.J. Bart, N. Giordano, A spectroscopic investigation of cerium molybdenum oxides, Journal of the Chemical Society, Dalton Transactions (1983) 1825–1829.

[68] N. Gunasekaran, S. Rajadurai, J.J. Carberry, N. Bakshi, C.B. Alcock, Surface characterization and catalytic properties of La1−xAxMO3 perovskite type oxides. Part I. Studies on La0.95Ba0.05MO3 (M = Mn, Fe or Co) oxides, Solid State Ionics 73 (1994) 289–295.

[69] K. Kishi, Y. Motoyoshi, S. Ikeda, Deposition of nickel from Ni(CO)4 on palladium and iron surfaces studied by X-ray photoelectron spectroscopy, Surface Science 105 (1981) 313–324.

[70] M.L. Rojas, J.L.G. Fierro, L.G. Tejuca, A.T. Bell, Preparation and characterization of LaMn1−xCUxO3+λ perovskite oxides, Journal of Catalysis 124 (1990) 41–51.

[71] C.E. Dubé, B. Workie, S.P. Kounaves, A. Robbat, M.L. Aksub, G. Davies, Electrodeposition of Metal Alloy and Mixed Oxide Films Using a Single-Precursor Tetranuclear Copper-Nickel Complex, Journal of The Electrochemical Society 142 (1995) 3357.

[72] C. Lv, H. Chen, M. Hu, T. Ai, H. Fu, Nano-oxides washcoat for enhanced catalytic oxidation activity toward the perovskite-based monolithic catalyst, Environmental Science and Pollution Research 28 (2021) 37142–37157.

[73] J.F. Moulder, W.F. Stickle, P.E. Sobol, Handbook of X-ray photoelectron spectroscopy: a reference book of standard spectra for identification and interpretation of XPS data, Physical Electronics,Inc., Eden Prairie, Minn, 1995.

[74] A.E. Bocquet, A. Fujimori, T. Mizokawa, T. Saitoh, H. Namatame, S. Suga, N. Kimizuka, Y. Takeda, M. Takano, Electronic structure of SrFe4+O3 and related Fe perovskite oxides, Phys Rev B Condens Matter 45 (1992) 1561–1570.

[75] V.I. Nefedov, M.N. Firsov, I.S. Shaplygin, Electronic structures of MRhO2, MRh2O4, RhMO4 and Rh2MO6 on the basis of X-ray spectroscopy and ESCA data, Journal of Electron Spectroscopy and Related Phenomena 26 (1982) 65–78.

[76] N.S. McIntyre, M.G. Cook, X-ray photoelectron studies on some oxides and hydroxides of cobalt, nickel, and copper, Analytical Chemistry 47 (1975) 2208–2213.

[77] V. Nemoshkalenko, V. Didyk, V. Krivitskii, A. Senkevich, Study of the charge state of atoms in iron, cobalt and nickel phosphides, Zhurnal neorganicheskoi khimii 28 (1983) 2182–2186.

[78] T. Dickinson, A.F. Povey, P.M.A. Sherwood, Dissolution and passivation of nickel. An X-ray photoelectron spectroscopic study, Journal of the Chemical Society, Faraday Transactions 1: Physical Chemistry in Condensed Phases 73 (1977) 327–343.

[79] L. He, Y. Shu, W. Li, M. Liu, Preparation of La0.7Sr0.3CoO3-δ (LSC)@MnO2 core/shell nanorods as high-performance electrode materials for supercapacitors, Journal of Materials Science: Materials in Electronics 30 (2019) 17–25.

[80] I. Alstrup, I. Chorkendorff, R. Candia, B.S. Clausen, H. Topsøe, A combined X-Ray photoelectron and Mössbauer emission spectroscopy study of the state of cobalt in sulfided, supported, and unsupported Co-Mo catalysts, Journal of Catalysis 77 (1982) 397–409.